

# Polarisation of THz synchrotron radiation: from its measurement to control

Meguya Ryu,<sup>1</sup> Denver Linklater,<sup>2</sup> William Hart,<sup>2</sup> Armandas Balčytis,<sup>2</sup> Edvinas Skliutas,<sup>3</sup> Mangirdas Malinauskas,<sup>3</sup> Dominique Appadoo,<sup>4</sup> Yaw-Ren Eugene Tan,<sup>5</sup> Junko Morikawa,<sup>1</sup> and Saulius Juodkazis<sup>2,6</sup>

<sup>1</sup>*Tokyo Institute of Technology, Meguro-ku, Tokyo 152-8550, Japan*

<sup>2</sup>*Swinburne University of Technology, John st., Hawthorn, Victoria 3122, Australia*

<sup>3</sup>*Laser Research Center, Department of Quantum Electronics, Faculty of Physics, Vilnius University, Saulėtekio Ave. 10, Vilnius LT-10223, Lithuania*

<sup>4</sup>*Infrared Microspectroscopy Beamline, Australian Synchrotron, Clayton, Victoria 3168, Australia*

<sup>5</sup>*Australian Synchrotron, Clayton, Victoria 3168, Australia*

<sup>6</sup>*Melbourne Center for Nanofabrication, Australian National Fabrication Facility Clayton, Victoria 3168, Australia*

(Dated: September 24, 2018)

Polarisation analysis of synchrotron THz radiation was carried out with a standard stretched polyethylene polariser and revealed that the linearly polarised (horizontal) component contributes up to  $22 \pm 5\%$  to the circular polarised synchrotron emission extracted by a gold-coated mirror with a horizontal slit inserted near a bending magnet edge. Comparison with theoretical predictions shows a qualitative match with dominance of the edge radiation. Grid polarisers 3D-printed out of commercial acrylic resin were tested for the polariser function and showed spectral regions where the dichroic ratio  $D_R > 1$  and  $< 1$  implying importance of molecular and/or stress induced anisotropy. Metal-coated 3D-printed THz optical elements can find a range of applications in intensity and polarisation control of THz beams.

PACS numbers: polarisation, FT-IR, synchrotron, anisotropy of absorbance, 3D printing

## I. INTRODUCTION

Methods of terahertz generation are evolving fast using ultra-short laser pulses, electrically driven 2D electron gas in semiconductor junctions, and photo-mixing, laser-driven electron plasmas to facilitate number of applications which require smaller and portable devices<sup>1-7</sup>. The highest intensity THz sources are available at free electron laser and synchrotron facilities<sup>8,9</sup>. With a high-brilliance synchrotron THz radiation it is possible to use imaging arrays and monitor *in situ* temporal evolution, e.g., of a phase transition in real time. Polarisation of synchrotron THz radiation becomes important in absorbance spectroscopy and for investigation of orientational anisotropy<sup>10,11</sup>. Even for non-absorbing transparent materials at THz spectral range, a birefringence would cause polarisation changes due to a purely refractive phase delay which is important for interpretation of spectroscopical data. Synchrotron THz wavelengths are spanning wavenumber range  $7-700 \text{ cm}^{-1}$  (or  $0.2 - 21 \text{ THz}$ ), which in terms of wavelengths are  $1.43 \text{ mm} - 14.3 \mu\text{m}$ . With a widely accessible 3D printing technology reaching tens-of-micrometers resolution of plastic components, there is a potential to make optical elements for THz applications. Rough surfaces on  $\sim 5 - 10 \mu\text{m}$  scale on 3D printed surfaces can be smoothed by controlled reflow using strongly absorbed UV post-illumination of the plastic workpieces<sup>12</sup> and are reaching required sub-wavelength  $\lambda/10$  min-max roughness even for the visible-IR spectral range applications. Plastics have refractive index of  $\sim 1.5$  at far-IR - to - THz spectral range with a variable absorbance, which has to be small for highly efficient optical elements<sup>13</sup>. Molecular ordering in

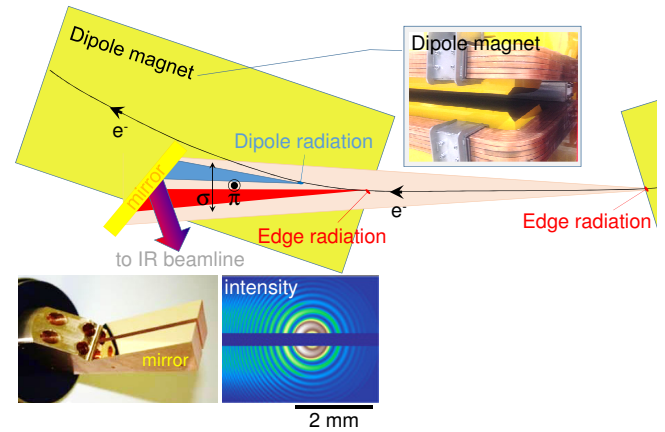


FIG. 1: Source of dipole and edge radiation which both have  $\sigma$  (horizontal along the slit) and  $\pi$  (vertical) components collected for the use at the IR beamline. Further along the beamline there is a beam splitter box that then directs the dipole radiation to the mid-IR branch of the beamline and the edge radiation to the far-IR branch. Pickup of THz radiation is made with the first mirror (photo). Intensity shows distribution of IR-THz radiation at the first mirror reflection.

polymers cause birefringence and an anisotropy of absorbance, which can be determined by the four polarisation method<sup>14</sup> used in this study.

Polarisation of synchrotron THz radiation has a complex structure which has to be well understood when beam is focused (or imaged) onto the sample with spot sizes down to sub-1 mm from the first mirror where the beam has cross sections of  $\sim 2 \text{ cm}$ . The synchrotron

THz radiation is created by relativistic electrons traveling through a dipole magnet.

The observed radiation from a dipole magnet in the orbital plane of the electron is referred to as  $\sigma$ -polarisation mode radiation and is typically horizontally polarised. In the perpendicular plane with a non-zero vertical observation angle,  $\psi$ , we have the  $\pi$ -polarisation mode radiation and is typically vertically polarised. The combination of the  $\sigma$  and  $\pi$  modes results in elliptically polarised radiation above and below the deflection plane of the electron beam (Fig. 1). The proportion of the integrated power of the  $\sigma$  mode to  $\pi$  mode radiation is,  $P_\sigma = \frac{7}{8}P_{tot}$  and  $P_\pi = \frac{1}{8}P_{tot}$  for typical dipole radiation<sup>15</sup>.

The THz spectrum of the synchrotron radiation used by the far-IR branch of the IR beamline at the Australian Synchrotron (AS) has a horizontal acceptance of -14 mrad to +14 mrad and focuses on using the radiation created by the electron beam just as it exits and enters the magnetic field of the dipole magnet<sup>16,17</sup>. This is referred to as edge radiation. The spatial and wavelength dependent distribution of the linearly and elliptically polarised radiation is more complex at the edge than in the body of the dipole magnet<sup>15,18</sup> and is discussed in Sec. III B.

In THz spectral range, it is possible to use linear polarisers to set polarisation at the sample with metallic grid or metallic gratings with high extinction ratio defined by transmission for the transverse magnetic and electric modes  $E_r = T_{TM}/T_{TE} \simeq 45$  dB at 1 THz<sup>19</sup>. This is achieved at the cost of a reduced intensity. By phase and polarisation control with 3D-printed optical elements with small absorption losses, it would be possible to create more efficient optical elements for polarisation control.

Here, we report results of a polarisation study of THz synchrotron radiation and characterisation of 3D-printed acrylic grid waveplate polarisers. Simulation of polarisation at the bending magnet edge is compared with experimental measurements at the sample location.

## II. METHODS

Polarisation analysis of synchrotron radiation was carried out at the IR Beamline on Australian Synchrotron, Melbourne<sup>21,22</sup> with a standard linear stretched polyethylene (PE) polariser (Bruker No. F251; 45- $\mu$ m-thick PE). Figure 2 shows schematics of experiments for polarisation analysis and absorbance anisotropy measurements of the 3D-printed micro-gratings.

### A. 3D-printed THz optical elements

Plastic gratings of varying aspect ratio (the depth-to-width)  $AR = d/w$ , duty cycle  $DR = w/P$  and period  $P$  (see geometry in Fig. 2(b)) were fabricated using the Ember 3D printer (AutoDesk). The Ember printer possesses

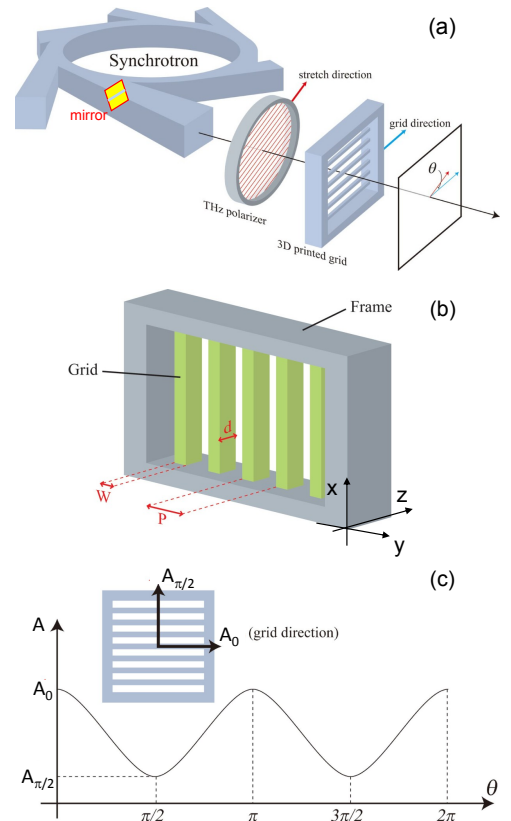


FIG. 2: (a) Geometry of experiment designed to characterise polarisation of the THz radiation by mirror with 3-mm-wide mid-gap. (b) 3D printed grating used as polarisers. (c) Expected angular dependence of the absorbance,  $A = -\lg T$ , from sample with orientational anisotropy.

a 405 nm wavelength light emitting diode (LED) source and a Texas Instruments digital micro-mirror (DMD) projection system which facilitates the UV-curing of an entire  $s = (10-100)$   $\mu$ m layer over a single exposure. The Ember 3D printer is capable of an xy-resolution of 50  $\mu$ m, and a z-resolution of 10-100  $\mu$ m. Gratings were set in a frame to allow them to be fixed to a polarisation filter mount. Grating width  $w$  ranged between 100-200  $\mu$ m, period  $P$  varied between 100-400  $\mu$ m, aspect ratio ranged from 1 to 4 and duty cycle was adjusted between 25%, 33% and 50%.

Commercially available MakerJuice G+ (red) and SF (green) resins were obtained from MakerJuice Labs, US. They are UV-curable acrylate-based resins with low viscosity and fast-curing capabilities. Also, a proprietary Ember resin (black) was used as supplied or was mixed from constituent ingredients, however, grids were less well developed due to a non-resolved parts of the unexposed segments.

Design files and stereo-lithography STL model files were generated using OpenSCAD ([www.openscad.org](http://www.openscad.org)), a parametric CAD program. A custom C# application was used to automatically generate a range of de-

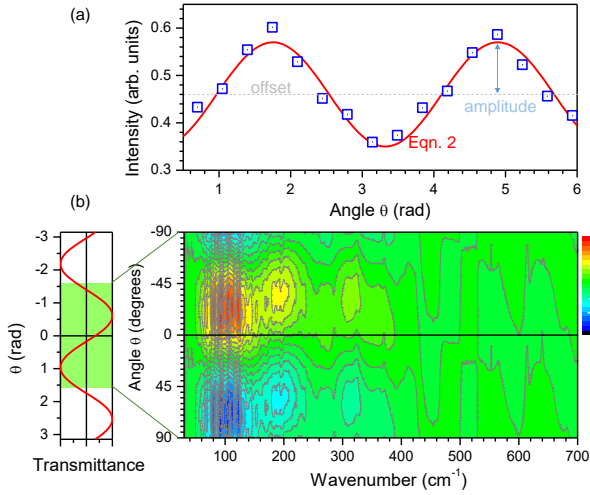


FIG. 3: (a) Experimental orientational dependence of synchrotron radiation transmission (squares) through the polyethylene polariser and the best fit by Eqn. 2; the phase was chosen for the best fit. (b) Spectrum-polarisation map of synchrotron radiation (the offset subtracted).

sign files and STL model files within the design space. To print gratings with a large phase retardance or absorbance along propagation of the THz beam ( $z$ -axis; Fig. 2(b)), the printing sequence followed stacked exposures as samples are moved along the  $x$ -axis. Using Autodesk software, Print Studio, sample files were oriented perpendicular to the build-head to allow sequential stacking of model layers, “growing” the grating in a layer by layer mode as the build-head is rotated across the resin tray, and lifted step-wise after the exposure of each model layer. Gratings were printed in  $25\ \mu\text{m}$  layers, with a 5 s exposure time for 4 burn-in layers, 8 s exposure for the first layer and 1.4 s exposure per each subsequent  $25\ \mu\text{m}$  layer. The print speed of  $25\ \mu\text{m}$  layers was 18 mm/h. The build head was optionally covered in Kapton tape to assist removal of the samples. 3D printed gratings were detached from the build head, then rinsed in a sequence of acetone, isopropanol and water to remove uncured resin.

For comparison of polariser performance, 3D-printed grids were coated with a 100 nm sputtered gold film. Such gratings can be considered having no transmission in the beam region for the light polarised along  $\theta = 0$  azimuth (a strong extinction due to reflection and absorption) and simulates performance of the gratings with  $AR = \infty$ .

## B. Optical characterisation

The dichroic ratio is defined by the maximum-to-minimum absorbance ratio  $D_r \equiv A_0/A_{\pi/2}$ , where  $A_{0,\pi/2}$  are absorbance values at two perpendicular orientation

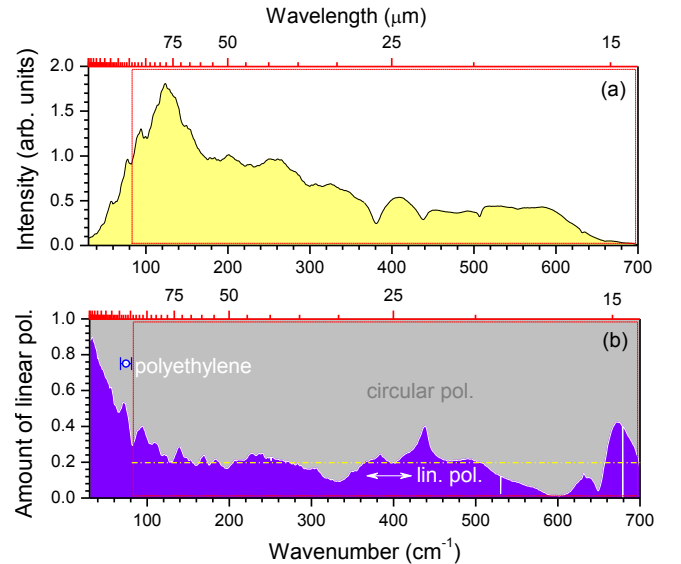


FIG. 4: (a) THz radiation spectrum (unpolarised). (b) Portion of the linearly polarised component  $Lin$  (Eqn. 3.) The spectral position of the absorption band of polyethylene at  $2.23 \pm 0.2\ \text{THz}^{20}$  is shown by the circular marker. Horizontal line at  $Lin \simeq 0.22$  defines the average contribution of the linearly polarised (horizontal) component of E-field. The region enclosed in the box is where transmittance of the polyethylene polariser is constant.

angles  $\theta$ . The  $D_r$  was determined for differently prepared 3D-printed grid polarisers; see, the plot is for the absorbance,  $A$ , in Fig. 2(c). When  $D_r = 1$  material (pattern) has isotropic absorbance while the metallic grid polariser has  $D_r > 1$  as the E-field of light polarised along the metallic lines of the grid is absorbed while the absorbance  $A_{\pi/2}$  is smaller. The case of  $D_r < 1$  would correspond to an anisotropy induced by a particular molecular alignment or internal stress in a grating-like pattern. The anisotropy of absorbance can be determined from the angular dependence of  $A_\theta$  and only four angles with angular separation of  $\pi/2$  are required to retrieve the fit as shown in Fig. 2(c)<sup>14</sup>:

$$A_\theta = A_0 \cos^2(\theta) + A_{\pi/2} \sin^2(\theta). \quad (1)$$

This method was recently used to determine anisotropy of absorbance of silk at mid-IR spectral range<sup>11</sup>.

## III. RESULTS AND DISCUSSION

### A. Polarisation of synchrotron THz radiation

Synchrotron THz radiation is extracted from the edge of a dipole magnet using a mirror with a 3-mm-wide slit (Fig. 1(b)) to allow higher energy photons to pass through. The resulting elliptically polarised radiation can be separated into a circularly polarised (isotropic)

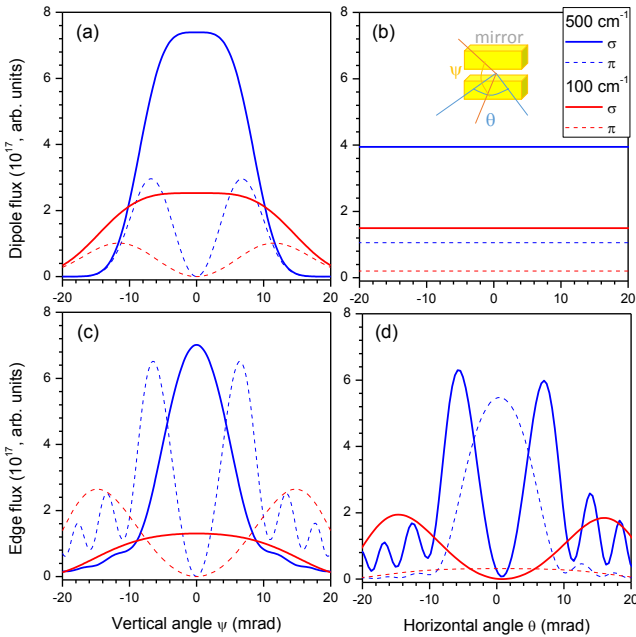


FIG. 5: (a) and (c) Compares the  $\sigma$  and  $\pi$  modes for  $100 \text{ cm}^{-1}$  and  $500 \text{ cm}^{-1}$  as a function of the vertical observation angle,  $\psi$  while (b) and (d) shows the change a function of the horizontal observation angle (in the plane of the electron beam),  $\theta$ . The comparison highlights the complex nature of the edge radiation. Inset in (b) schematically shows the first mirror and angular spread of the IR-THz beam extracted into the beamline.

component of the light field  $E_I$  and a linear component  $E_L$  aligned with the horizontal slit ( $\theta = 0^\circ$  azimuth). Figure 1(b) shows intensity distribution of the synchrotron radiation beam taken to the IR beamline. A standard linear stretched polyethylene polariser was set into the beam at normal incidence and its orientation,  $\theta$ , was changed by a motorized stage while measuring transmission (Fig. 1(b)).

Figure 3(a) shows the angular dependence of transmission,  $T(\theta)$  measured with  $20^\circ$  orientation steps and the best fit to the Malus law  $\propto \cos^2(\theta)$  for the analysed case as shown below. For this case of horizontally polarised linear component  $E_L$  ( $\theta = 0^\circ$ ) mixture with the isotropically (circularly) polarised field,  $E_I$ , lets establish an orthogonal base with E-fields at two azimuths  $\theta = 0$  and  $\theta = \pi/2$ ,  $E_{0,\pi/2}$ , respectively, for the output (transmitted) intensity  $E_\theta^2$ :

$$\begin{aligned} E_\theta^2 &= E_0^2 \cos^2(\theta) + E_{\pi/2}^2 \sin^2(\theta) \\ &= \left( \frac{1}{2} E_I^2 + E_L^2 \right) \cos^2(\theta) + \frac{1}{2} E_I^2 \sin^2(\theta) \\ &= \frac{1}{2} (E_I^2 + E_L^2) + \frac{1}{2} E_L^2 \cos(2\theta), \end{aligned} \quad (2)$$

where  $I_{off} = \frac{1}{2}(E_I^2 + E_L^2)$  is the offset intensity and  $I_{amp} = \frac{1}{2}E_L^2$  is the amplitude of the transmitted light

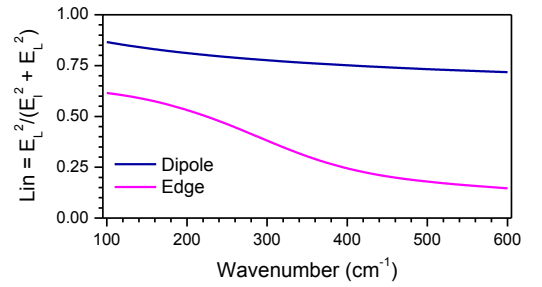


FIG. 6: Simulation data showing contribution of the linear polarisation (horizontal; along the first mirror slit, Eqn. 3); modeling is shown in Fig. 5 at selected wavenumbers. Difference in spectral dependencies of  $Lin$  ratio shown for the dipole and edge radiations. Radiation is integrated over the vertical observation angle,  $\psi$  from  $-8.5$  to  $+8.5$  mrad and horizontally over  $\theta$  from  $-14$  to  $14$  mrad.

(through the analyser). The best fit to  $\cos(2\theta)$  dependence according to Eqn. 2 provides  $I_{off}$  and  $I_{amp}$  values. By measuring angular dependence of the transmission spectrum, it is possible to present a map which shows spectrum in abscise and orientation in the ordinate directions (Fig. 3(b)). It is revealed that the used polariser has a spectrally broadband action over the entire THz window (Fig. 3(b)).

Exact portion of the linearly polarised light in the entire spectrum (Fig. 4(a)) is estimated by the factor:

$$Lin \equiv \frac{E_L^2}{E_L^2 + E_I^2} = \frac{I_{amp}}{I_{off}}, \quad (3)$$

which is plotted in Fig. 4(b) and obtained as the best fit to experimental data at fixed wavelength using  $I_{amp}$  and  $I_{off}$  parameters. At the most intense THz spectral range it was close to 22%. The highest linearly polarised intensity is obtained at  $\theta = 0^\circ$ , horizontally with the first mirror slit.

## B. Edge radiation

A diagram of the source of synchrotron radiation for the IR beamline is shown in Fig. 1. The spatial and spectral distribution of the synchrotron radiation from a dipole magnet is well understood and using the equations from ref.<sup>23</sup> the integrated flux of the  $\sigma$  and  $\pi$  polarisations of radiation were simulated.

The dipole radiation is extracted with a rectangular mirror ( $30 \times 54 \times 460$  mm; Fig. 1(b)) located  $\sim 1.3$  m downstream from the edge of the dipole magnet designed with an acceptance of  $58$  mrad in the horizontal plane ( $-14$  mrad to  $+44$  mrad) and  $17$  mrad vertically<sup>24,25</sup>. Matching of numerical apertures of the radiation gathering optics along the entire beamline also plays an important role. The *étendue*,  $\varepsilon$ , is a measure of the flux gathering capability of the optical system, i.e., the col-

lected power is the product of  $\varepsilon = \text{area} \times \text{solid angle}$  [ $\text{m}^2\text{sr}$ ] and the radiance of the source [ $\text{W}/\text{m}^2/\text{sr}$ ].

In Fig. 5 the comparison clearly highlights the complex nature of the edge radiation and is sensitive to the exact profile of the magnetic field at the edge of the dipole magnet. These simulations only account for the distribution of radiation from a single electron, while for exact simulation it would need to factor in the cross section of the electron beam ( $\sigma_x, \sigma_{x'}, \sigma_y, \sigma_{y'}$ )<sup>18</sup>. Using this single electron model and describing the elliptical radiation as a combination of linear and circular polarisations (as presented in Eqn. 3) Fig. 6 compares how the ratio of linear to circular polarisation changes as a function of wavenumbers for the dipole and edge radiation. A larger contribution of the horizontal linear polarisation at small wavenumbers is characteristic for both the dipole and edge radiation. The measured polarisation ratio  $Lin$  at the sample location (Fig. 4(b)) shows a smaller portion of the linear polarisation due to the *étendue*,  $\varepsilon$ , and potentially reflects the unmatched numerical apertures for radiation collection. However, the same trend of larger contribution of linear (horizontal) polarisation at low wavenumbers ( $< 100 \text{ cm}^{-1}$ ) as theoretically predicted was experimentally observed.

### C. 3D printed polariser grids

With the fully determined polarisation of the THz radiation, 3D-printed optical elements (Fig. 7(a)) were characterised using the same setup shown schematically in Fig. 2 for different duty cycle and aspect ratio acrylic elements. Figure 7(b) shows dependence of the dichroic ratio  $D_r = A_{max}/A_{min} \propto T_{min}/T_{max}$  vs. wavelength. The  $D_r$  was increasing for longer wavelengths as would be expected for a grid-type polariser where E-field component along the grid beams is absorbed stronger. This effect was not very strong since  $P > \lambda$ , however, the tendency is clearly recognisable and is more expressed for the higher aspect ratio grids (more absorbance). As the  $AR$  was increasing a tendency of  $D_r < 1$  emerged at specific 30-40  $\mu\text{m}$  wavelength region (Fig. 7(b)). Anisotropy in molecular alignment is an expected cause (can be linked to the stress in the printed grid). Similarly, the speed of silk formation is defining molecular alignment and mechanical strength of silk brins<sup>26-28</sup>. The optical birefringence and activity due to an orientational anisotropy is also linked to anisotropy of absorbance and is one of the consequences of the molecular alignment<sup>29</sup>.

Usually, the optimum duty cycle for polarisation optics and phase retardance  $\Delta n \times d$  is at  $DR = 0.5$  when sub-wavelength gratings are fabricated; here  $\Delta n$  is birefringence. This directly follows from the effective medium theory (EMT) which shows that the smallest height structures required to effectively phase delay the beam have the minimal height. This usually corresponds to a desired fabrication condition. Since the EMT can not be used for the case discussed here with  $P > \lambda$ , the

efficient phase control cannot be achieved. The dichroic ratio shown in Fig. 8 is close to  $D_r \sim 1$  corresponding to optically isotropic material for absorption. Only for the largest duty cycle  $DR = 0.5$  an anisotropy begin to be apparent  $D_r > 1$ , again as wavelength is increased closer to the EMT range (Fig. 8(a)). By sputtering 100 nm of gold, the 3D-printed grating has to become more anisotropic since THz E-field component parallel to the grid beams should be absorbed in metal; this can be considered equivalent to an increase of the aspect ratio  $AR \rightarrow \infty$ . However, the effect of  $D_r > 1$  was not strongly pronounced. This can be understood as being caused by  $P > \lambda$ .

Dichroic losses measured of a grating for two linearly polarised beam orientations  $e^{-\Delta} = \sqrt{P_{\parallel}/P_{\perp}}$  provides an indirect measure whether material is suitable for fabrication of phase elements, optical retarders to control phase, polarisation, focusing, and orbital momentum. The achievable efficiency of an optical element, from

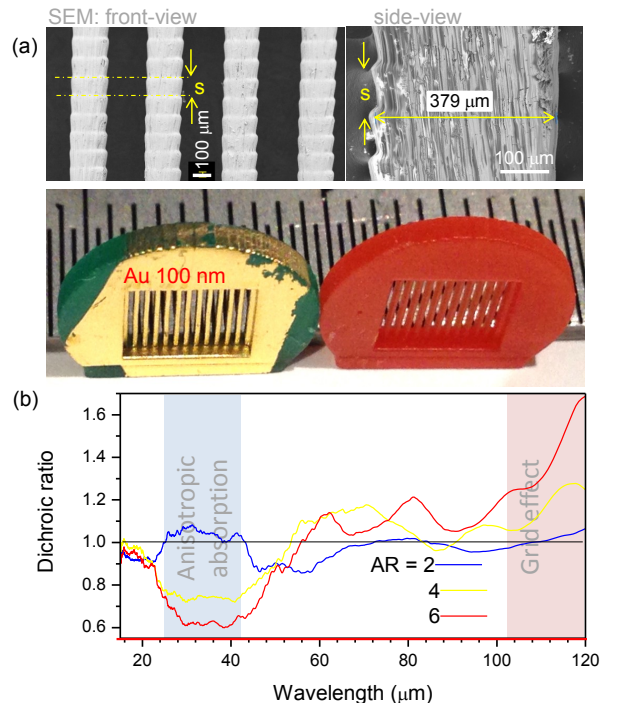


FIG. 7: (a) SEM front- and side-view images of a 3D-printed grating and photo images of typical samples made out of MakerJuice G+ (red) and SF (green) resins;  $s$  is the thickness of layer made in one exposure. Time required to print one sample was  $\sim 5$  min; sample is moved upwards with layers added at the bottom. (b) The dichroic ratio  $D_r = A_{max}/A_{min} \propto T_{min}/T_{max}$  (in other conventions  $D_r = A_{\parallel}/A_{\perp} = A_{\parallel}/A_{\perp}$ ) vs. wavelength for acrylic 3D-printed gratings of several aspect ratios  $AR = \frac{d}{w}$ ; period  $P = 400 \mu\text{m}$ , duty ratio  $DR = \frac{w}{P} = 0.33$ . The same spectral window is enclosed in the box in Fig. 4. The color shaded regions mark spectral ranges where grid effect and anisotropy of absorption are pronounced.

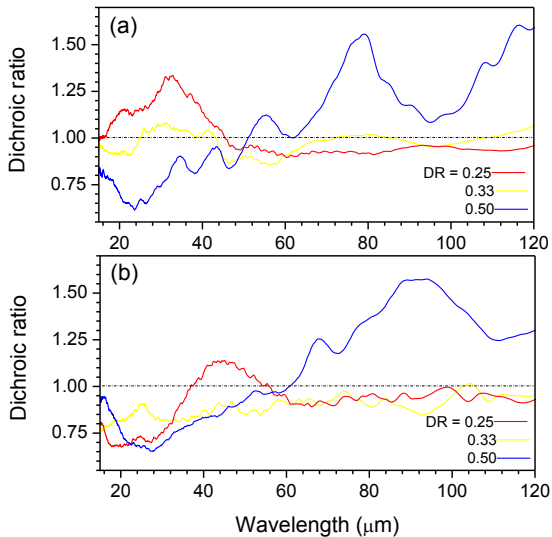


FIG. 8: The dichroic ratio  $D_r$  vs. wavelength for acrylic 3D printed grid without (a) and with (b) 100 nm gold coating for several duty ratios  $DR = \frac{w}{P}$ ; period  $P = 400 \mu\text{m}$ .

the material point of view, is related to the smallest losses defined by the imaginary part of refractive index ( $n' + in''$ ), which is linked to the retardance and dichroism by  $\Delta = \Delta' + i\Delta''$  with  $\Delta^{(', '')} = k[n_{\parallel}^{(', '')} - n_{\perp}^{(', '')}]d$ ; the retardance  $\Delta'$  and dichroism  $\Delta''$  of the  $d$  height optical element (e.g., grating) at wavevector  $k = 2\pi/\lambda$  for the wavelength  $\lambda$  governs the efficiency of the optical element. The amplitude of the E-field decreases exponentially with the height, i.e., the intensity is given by the Lambert-Beer's law  $I(h) = I_0 e^{-2n''\omega h/c} = I_0 e^{-\alpha(\omega)h}$ , where  $\alpha(\omega) = 2n''k$  is the absorption coefficient. Then, the amplitude,  $Amp$ , of the cos-wave-form measured by the 4-polarisation method (Eqn. 1) is related to the dichroism as:

$$Amp \equiv (A_{\parallel} - A_{\perp})/2 = k(n''_{\parallel} - n''_{\perp})h \equiv \Delta''. \quad (4)$$

For efficient absorbance and retardance control, 3D printing technology has to deliver  $P < \lambda$  precision of structuring which begins to be accessible at THz spectral band. Here we showed that open grid structures with high aspect ratio can be fabricated at the desired  $DR = 0.5$ , however, further decrease in the width of grating beam is required to obtain larger dichroic ratio  $D_r$ . The printing method demonstrated here allows 3D printing of gratings with arbitrary depth,  $d$ , of the structure.

#### IV. CONCLUSIONS AND OUTLOOK

Contributions of the linear and circular polarisation components in THz beamline spectrum have been deter-

mined using polarisation analysis of transmission.

3D-printed acrylic gratings with rod width of  $\sim 100 \mu\text{m}$  period, duty cycle 0.5, and aspect ratio up to 8 were made out of standard acrylic resin. Low absorbance of 3D-printed structures is promising for fabrication of phase control elements (optical retarders) which would open new set of polarisation control of THz beams. The ability to rapidly produce a wide range of complex optical elements using 3D printing from various materials (including biocompatible materials) is a key benefit of 3D printers such as Ember that further enhance this possibility. Polariser-analyser setup will be required to further investigate optical retardance due to phase delay in addition to the absorbance investigated in this study.

Phase control using different approaches tested for visible and near-IR spectral ranges are transferable to longer IR and THz frequencies. Usual phase control relies on defined thickness of material (the propagation phase)<sup>30</sup>, geometrical phase made by azimuthal patterning of orientation of the optical axis<sup>31</sup>, as well as using metamaterials with phase control by spectrally overlapping electric and magnetic dipoles in non-absorbing high-refractive index materials ( $n > 2$ )<sup>32</sup> which allow to engineer polarisation, intensity, and orbital angular momentum of the light. The latter two concepts can be considered as flat optics and can be combined with intensity control by axicon or Fresnel lens demonstrated recently for THz wavelengths with performance matching theoretical efficiency<sup>33</sup>. 3D structuring of Si surface by fs-laser direct oxidation with subsequent plasma etching opens new possibilities in THz optics where Si is transparent<sup>34,35</sup>.

#### Acknowledgements

Experiments were carried out via beamtime project No. 11615 at the Melbourne synchrotron on 8-11 March 2017. This work was performed in part at the Melbourne Centre for Nanofabrication (MCN) in the Victorian Node of the Australian National Fabrication Facility (ANFF). W.H. is supported by an Australian Government Research Training Program Scholarship. Partial support via NATO grant SPS-985048 "Nanostructures for Highly Efficient Infrared Detection" is acknowledged. E.S. and M.M. acknowledge financial support by the OPTIBIOFORM (S-LAT-17-2) project from the Research Council of Lithuania. J.M. acknowledges the support of JSPS KAKENHI Grant Number 16K06768. This work was supported in part by the Global University Project at Tokyo Institute of Technology.

- <sup>1</sup> W. R. Huang, A. Fallahi, X. Wu, H. Cankaya, A.-L. Calendron, K. Ravi, D. Zhang, E. A. Nanni, K.-H. Hong, and F. X. Kärtner, "Terahertz-driven, all-optical electron gun," *Optica* **3**(11), pp. 1209 – 1212, 2016.
- <sup>2</sup> G. L. Carr, M. C. Martin, W. R. McKinney, K. Jordan, G. R. Neil, and G. P. Williams, "High-power terahertz radiation from relativistic electrons," *Nature* **420**, pp. 153 – 156, 2002.
- <sup>3</sup> H. A. Hafez, X. Chai, A. Ibrahim, S. Mondal, D. Férachou, X. Ropagnol, and T. Ozaki, "Intense terahertz radiation and their applications," *J. Opt.* **18**, p. 093004, 2016.
- <sup>4</sup> Y. Tian, J. S. Liu, Y. F. Bai, S. Zhou, H. Y. Sun, W. W. Liu, J. Zhao, R. Li, and Z. Xu, "Femtosecond-laser-driven wire-guided helical undulator for intense terahertz radiation," *Nature Photonics* **11**, pp. 242 – 246, 2017.
- <sup>5</sup> M. Dyakonov and M. Shur, "Detection, mixing, and frequency multiplication of terahertz radiation by two-dimensional electronic fluid," *IEEE Transac. Electron Devices* **43**(3), pp. 380 – 387, 1996.
- <sup>6</sup> E. A. Nanni, W. R. Huang, K.-H. Hong, K. Ravi, A. Fallahi, G. Moriena, R. J. D. Miller, and F. X. Kärtner, "Terahertz-driven linear electron acceleration," *Nature Comm.* **6**, p. 8486, 2015.
- <sup>7</sup> V. Jakštas, I. Grigelionis, V. Janonis, G. Valušis, I. Kašalynas, G. Seniutinas, S. Juodkakis, P. Prystawko, and M. Leszczynski, "Electrically driven terahertz radiation of 2DEG plasmons in AlGaIn/GaN structures at 110 K temperature," *Appl. Phys. Lett.* **110**(20), p. 202101, 2017.
- <sup>8</sup> P. Tan, J. Huang, K. F. Liu, Y. Q. Xiong, and M. W. Fan, "Terahertz radiation sources based on free electron lasers and their applications," *Sci. China Inform. Sci.* **55**(1), pp. 1 – 15, 2012.
- <sup>9</sup> B. A. Knyazev, G. N. Kulipanov, and N. A. Vinokurov, "Novosibirsk terahertz free electron laser: instrumentation development and experimental achievements," *Meas. Sci. Technol.* **21**, p. 054017, 2010.
- <sup>10</sup> A. Balčytis, M. Ryu, X. Wang, F. Novelli, G. Seniutinas, S. Du, X. Wang, J. Li, J. Davis, D. Appadoo, J. Morikawa, and S. Juodkakis, "Silk: Optical properties over 12.6 octaves THz-IR-Visible-UV range," *Materials* **10**(4), p. 356, 2017.
- <sup>11</sup> M. Ryu, A. Balčytis, X. Wang, J. Vongsvivut, Y. Hikima, J. Li, M. J. Tobin, S. Juodkakis, and J. Morikawa, "Orientational mapping augmented sub-wavelength hyper-spectral imaging of silk," *arXiv preprint*, p. arXiv:1706.01302, 2017.
- <sup>12</sup> N. Chidambaram, R. Kirchner, R. Fallica, L. Yu, M. Altana, and H. Schift, "Selective surface smoothing of polymer microlenses by depth confined softening," *Adv. Mater. Technol.*, p. 1700018, 2017.
- <sup>13</sup> P. D. Cunningham, N. N. Valdes, F. A. Vallejo, L. M. Hayden, B. Polishak, X.-H. Zhou, J. Luo, A. K.-Y. Jen, J. C. Williams, and R. J. Twieg, "Broadband terahertz characterization of the refractive index and absorption of some important polymeric and organic electro-optic materials," *J. Appl. Phys.* **109**, p. 043505, 2011.
- <sup>14</sup> Y. Hikima, J. Morikawa, and T. Hashimoto, "FT-IR image processing algorithms for in-plane orientation function and azimuth angle of uniaxially drawn polyethylene composite film," *Macromolecules* **44**(10), pp. 3950 – 3957, 2011.
- <sup>15</sup> A. Balerna and S. Mobilio, *Introduction to Synchrotron Radiation*, ch. 1, pp. 3 – 28. Springer, 2015.
- <sup>16</sup> O. Chubar and N. Smolyakov, "Generation of intensive long-wavelength edge radiation in high-energy electron storage rings," in *Particle Accelerator Conference, 1993., Proceedings of the 1993*, pp. 1626–1628, IEEE, 1993.
- <sup>17</sup> O. Chubar and N. Smolyakov, "Vuv range edge radiation in electron storage rings," *J. Optics* **24**(3), p. 117, 1993.
- <sup>18</sup> O. Chubar, "Precise computation of electron-beam radiation in nonuniform magnetic fields as a tool for beam diagnostics," *Rev. Sci. Instr.* **66**(2), pp. 1872–1874, 1995.
- <sup>19</sup> I. Yamada, K. Takano, M. Hangyo, M. Saito, and W. Watanabe, "Terahertz wire-grid polarizers with micrometer-pitch Al gratings," *Opt. Lett.* **34**(3), pp. 274 – 276, 2009.
- <sup>20</sup> S. Sommer, T. Raidt, B. M. Fischer, F. Katzenberg, J. C. Tiller, and M. Koch, "THz-spectroscopy on high density polyethylene with different crystallinity," *J Infrared Milli Terahz Waves* **37**, pp. 189 – 197, 2016.
- <sup>21</sup> G. SLeBlanc, M. J. Boland, and Y. Tan, "The Australian synchrotron project storage ring and injection system overview," in *Proc. EPAC*, p. 2263 – 2265, 2004.
- <sup>22</sup> J. Boldeman and D. Einfeld, "The physics design of the Australian synchrotron storage ring," *Nuclear Instr. Methods Physics Res. Sec. A* **521**(2), pp. 306–317, 2004.
- <sup>23</sup> A. W. Chao, K. H. Mess, M. Tigner, and F. Zimmermann, *Handbook of accelerator physics and engineering*, 2013.
- <sup>24</sup> D. Creagh, J. McKinlay, and P. Dumas, "The design of the infrared beamline at the Australian synchrotron," *Vibr. Spectr.* **41**(2), pp. 213–220, 2006.
- <sup>25</sup> D. Creagh, M. Tobin, A. Broadbent, J. McKinlay, J.-Y. Choi, and S. Rah, "An infrared beamline at the Australian synchrotron," in *AIP Conf. Proc.*, **879**(1), pp. 615–618, AIP, 2007.
- <sup>26</sup> Z. Shao and F. Vollrath, "Surprising strength of silkworm silk," *Nature* **418**, p. 741, 2002.
- <sup>27</sup> N. Du, X. Y. Liu, J. Narayanan, L. Li, M. L. M. Lim, and D. Li, "Design of superior spider silk: From nanostructure to mechanical properties," *Biophysical J.* **91**, pp. 4528 – 4535, 2006.
- <sup>28</sup> T. Yoshioka, K. Tashiro, and N. Ohta, "Molecular orientation enhancement of silk by the hot-stretching-induced transition from  $\alpha$ -helix-HFIP complex to  $\beta$ -sheet," *Biomacromolecules* **17**(4), pp. 1437 – 1448, 2016.
- <sup>29</sup> Y. N. Chirgadze, S. Y. Venyaminov, and V. M. Lobachev, "Optical rotatory dispersion of polypeptides in the near-infrared region," *Biopolymers* **10**(5), pp. 809 – 820, 1971.
- <sup>30</sup> E. Basselet, M. Malinauskas, A. Žukauskas, and S. Juodkakis, "Photo-polymerized microscopic vortex beam generators : precise delivery of optical orbital angular momentum," *Appl. Phys. Lett.* **97**, p. 211108, 2010.
- <sup>31</sup> X. Wang, A. A. Kuchmizhak, E. Basselet, and S. Juodkakis, "Dielectric geometric phase optical elements fabricated by femtosecond direct laser writing in photoresists," *Appl. Phys. Lett.* **110**(18), p. 181101, 2017.
- <sup>32</sup> K. E. Chong, I. Staude, A. James, J. Dominguez, S. Liu, S. Campione, G. S. Subramania, T. S. Luk, M. Decker, D. N. Neshev, I. Brener, and Y. S. Kivshar, "Polarization-independent silicon metadevices for efficient optical wavefront control," *Nano Lett.* **15**(8), pp. 5369 – 5374, 2015.
- <sup>33</sup> L. Minkevičius, S. Indrišūnas, R. Šniaukas, B. Voisiat, V. Janonis, V. Tamošiūnas, I. Kašalynas, G. Račiukaitis,

and G. Valušis, “Terahertz multilevel phase Fresnel lenses fabricated by laser patterning of silicon,” *Opt. Lett.* **42**(10), pp. 1875 – 1878, 2017.

<sup>34</sup> X.-Q. Liu, L. Yu, Z.-C. Ma, and Q.-D. Chen, “Silicon three-dimensional structures fabricated by femtosecond laser modification with dry etching,” *Appl. Opt.* **56**(8),

p. 282887, 2017.

<sup>35</sup> X.-Q. Liu, L. Yu, Q.-D. Chen, and H.-B. Sun, “Mask-free construction of three-dimensional silicon structures by dry etching assisted gray-scale femtosecond laser direct writing,” *Appl. Phys. Lett.* **110**, p. 091602, 2017.